Supporting Information

Durable Zn-ion Hybrid Capacitors using 3D Printed Carbon Composites

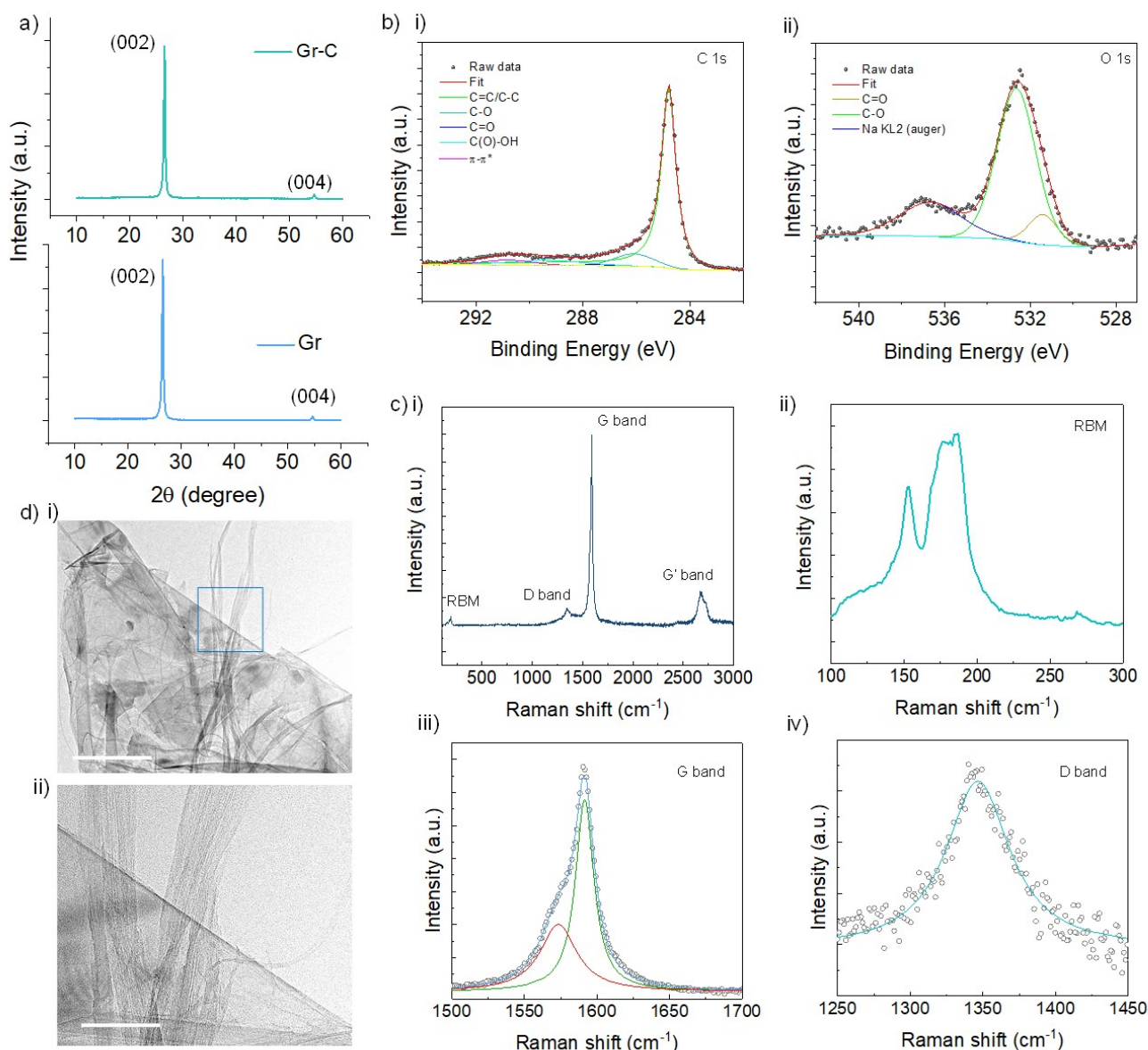Goli Nagaraju[1],[a] Stefano Tagliaferri[1],[a] Apostolos Panagiotopoulos[1], Mauro Och[1], Rachael Quintin-

Baxendale[1], and Cecilia Mattevi[1]*

[1]Department of Materials, Imperial College London, London SW7 2AZ, United Kingdom

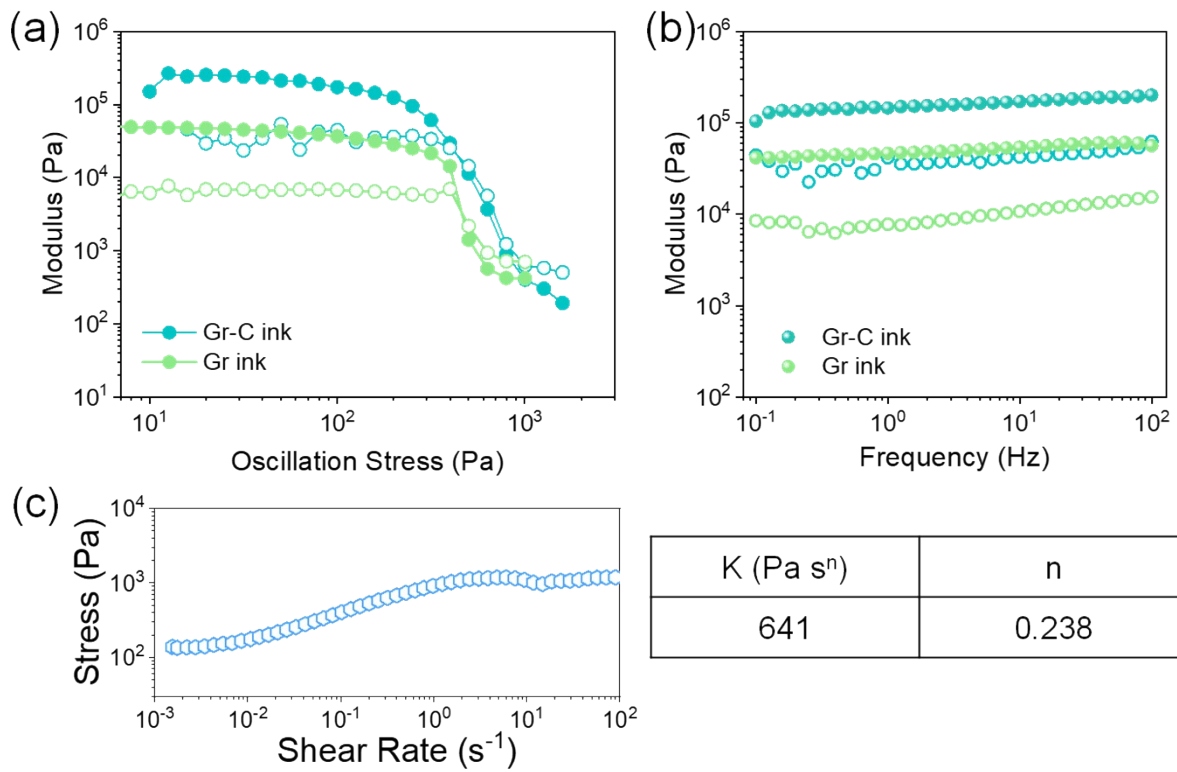[a] G.N. and S.T. equally contributed to this work

*Address correspondence to c.mattevi@imperial.ac.uk

Tel: +44(0) 2075940833

Figure S1. a) XRD diffractograms for the graphene and graphene-carbon nanotubes inks, XPS spectra (h=1253.6 eV) of b) (i) carbon 1s peak which has been deconvolved into 3 four contributions: C=C/C-C in aromatic rings (284.6 eV); C-O (286.1 eV); C=O (287.5 eV); C(O)-(OH) (289.2 eV); and π–π* satellite peak (290.6 eV). The dominant contribution is due to the sp2 carbon. and b) (ii) O 1s spectra at 531 eV of Gr-C sample after thermal treatment. A small contribution from the Auger Na KL2 is present at 537.5 eV. The spectra were fit by Doniach-Sunjic function after subtracting a Shirley background. c) Raman Spectra of the Gr-C composite, showing an intense vibrational mode at ~1590 cm^{-1} (G band) and a weaker vibrational mode at ~1346 cm^{-1} (D band), both characteristic of sp^2 carbon[1,2] (i). The G band is associated with the E_{2g} in-plane phonon mode at the Brillouin zone centre, whereas the D band stems from disorder-induced breathing modes of sp^2 atoms. The D- and G- bands were fitted using Lorentz functions (iii-iv). The ratio between the intensity of the D- and G-band is low ($I_D/I_G \sim 0.05$), indicating the good structural quality and low defect density in the Gr-C composite after ink formulation. The vibrational modes between 120 and 250 cm^{-1} are characteristic features of single walled carbon nanotubes (SWCNTs) with a diameter between ~0.7 and ~2 nm, arising from the radial breathing mode (RBM) of the nanotube sp^2 atoms[1,2]. The presence of SWCNTs in the composite ink is also visible from the G-band (iii), which consists of two partially convoluted peaks at ~1573 cm^{-1} (G$^-$) and ~1591 cm^{-1} (G$^+$), as a result of wave vector confinement in the circumferential direction and symmetry-breaking effects of the nanotube curvature. d) Low- (i) and

high-magnification (ii) TEM images of Gr-C composite, showing two-dimensional Gr platelets interconnected with numerous bundles of CNTs forming the network-like and interconnected heterostructures (scale bars: 500 and 100 nm, respectively).

(a)

Modulus (Pa) vs Oscillation Stress (Pa)

- Gr-C ink
- Gr ink

(b)

Modulus (Pa) vs Frequency (Hz)

- Gr-C ink
- Gr ink

(c)

Stress (Pa) vs Shear Rate (s^{-1})

K (Pa s^n)	n
641	0.238

Figure S2. a,b) Comparison of the rheological properties of the composite Gr-C ink and the Gr ink (containing no CNTs): a) oscillatory amplitude sweep and b) oscillatory frequency sweep in the linear viscoelastic region; c) Flow curve for the Gr-C ink (left) and results of the power-law fitting of the viscosity curve (right).
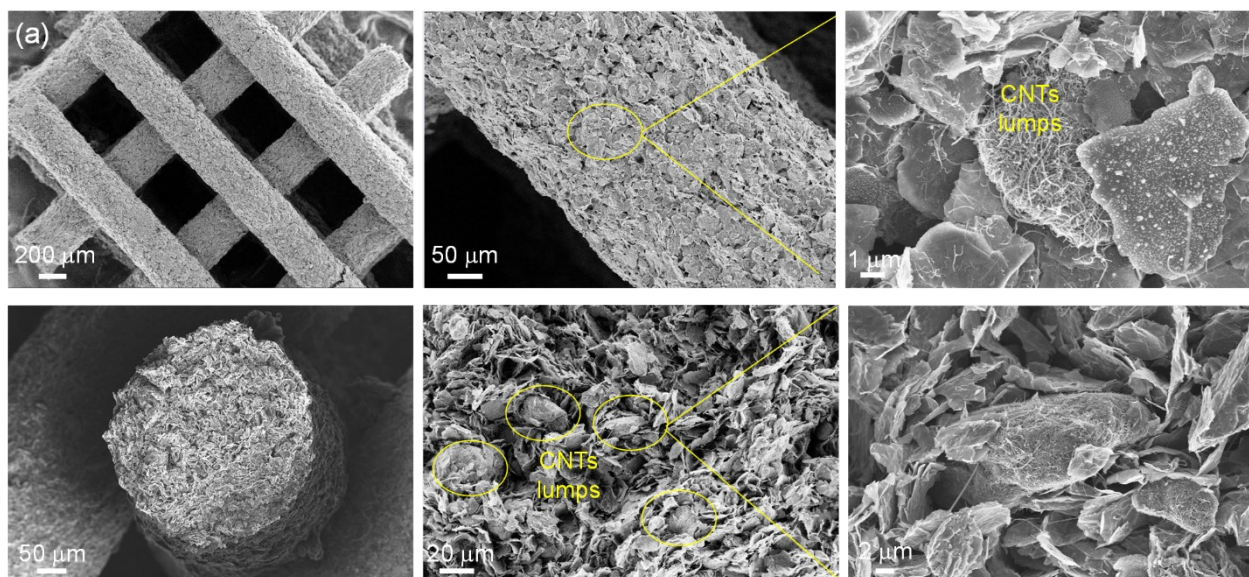
Figure S3. Low- and magnified FE-SEM images of Gr-C electrodes prepared using CNTs powder. For the ink preparation, 5% of CNTs powder was added to 95% of Gr platelets and CMC binder in DI-water to form a Gr-C ink. After printing and drying the Gr-C electrode, the chunks-like CNTs were observed in printed Gr electrodes. The mass gathering of CNTs lumps were mainly due to the strong van der Waals interactions and high hydrophobic nature of CNTs.
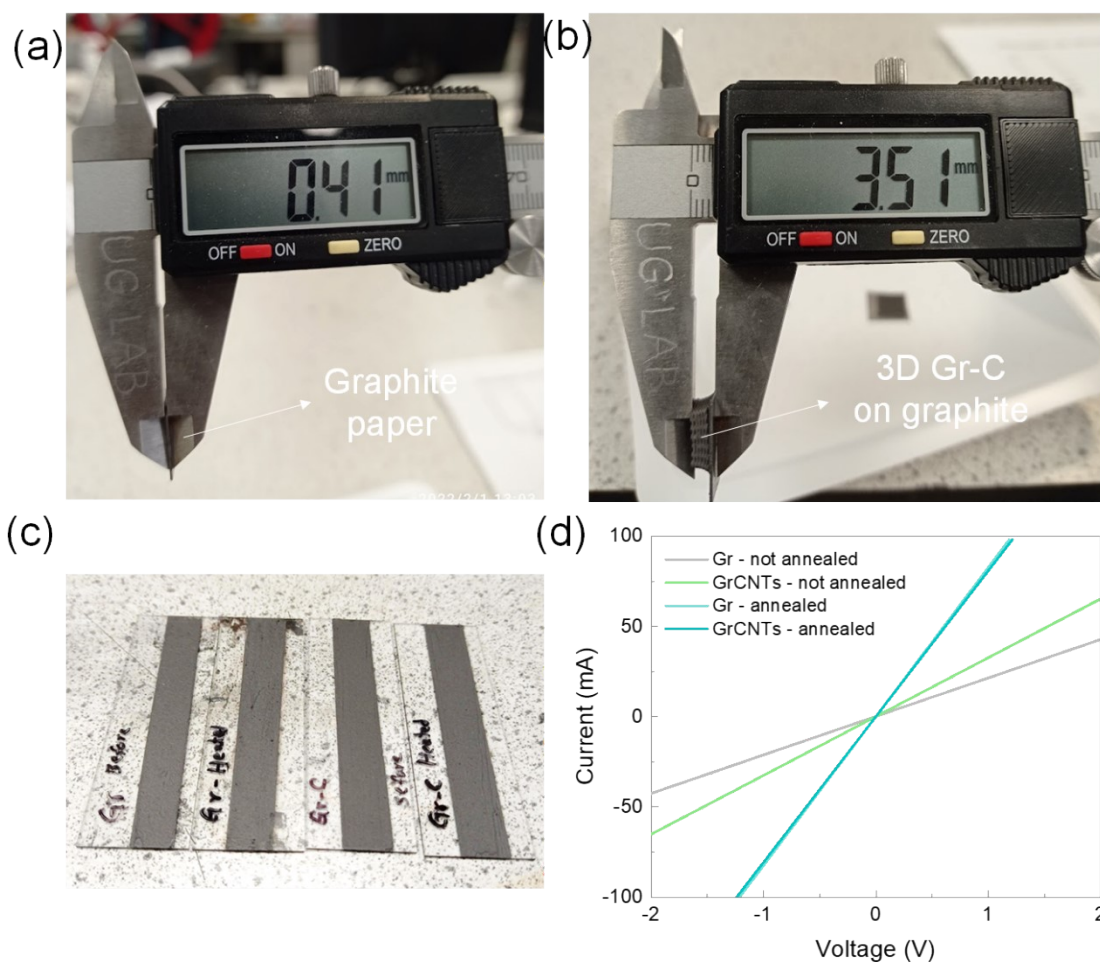
Figure S4. Digital photographs demonstrating the width (in mm) of (a) pristine graphite foil and b) 3D printed Gr-C on graphite foil obtained by Vernier scale. (c) Photographs of thin-film Gr- and Gr-C inks coated on glass (before and after annealing) for electrical conductivity measurements. (d) I-V curves of Gr- and Gr-C thin film electrodes measured using four-probe measurements.
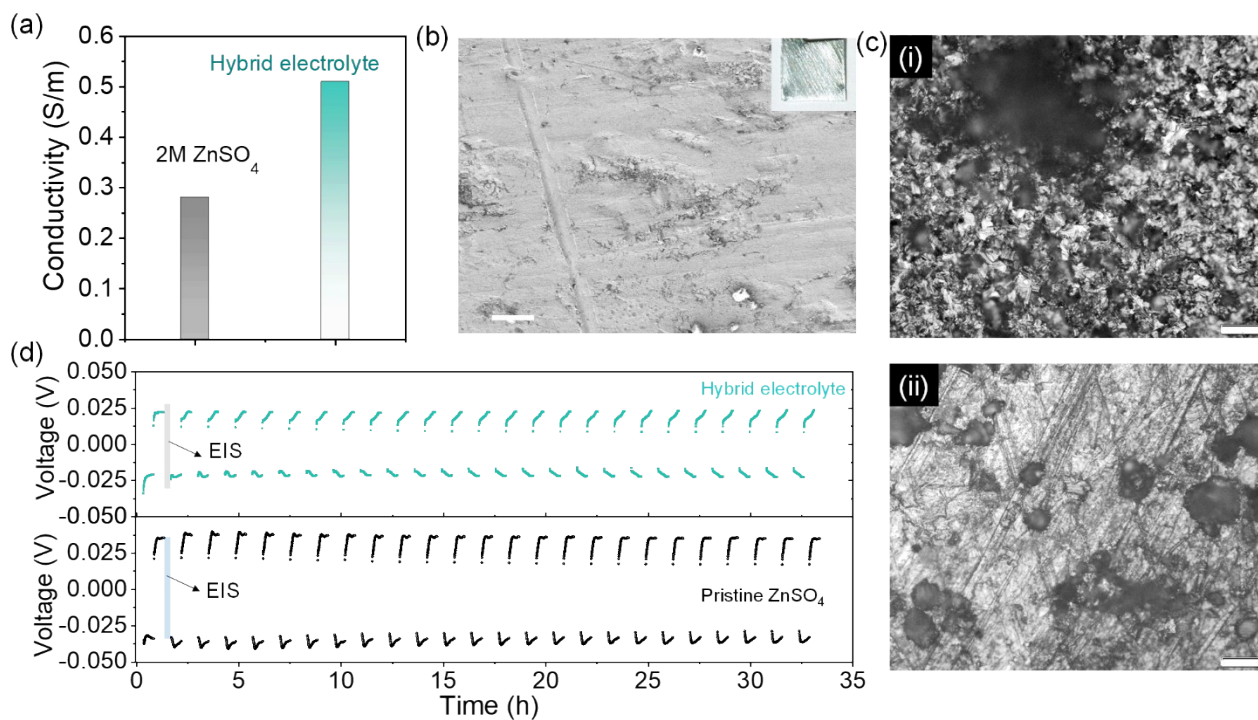
Figure S5. (a) Ionic conductivity of pristine 2M $ZnSO_4$ and 2M $ZnSO_4$+NaCl hybrid electrolyte obtained using two-probe measurements. (b) SEM image of pristine Zn foil before cycling (scale bar: 20 µm). The inset of b) shows the digital photograph of pristine Zn foil before cycling. c) optical microscope images (scale bar: 50 µm) of the Zn metal after plating/stripping test in (i) pristine and (ii) hybrid electrolyte. (d) Chronopotentiometry stripping/plating process of Zn//Zn cells in pristine $ZnSO_4$ and hybrid electrolyte. The time delay (marked with 'arrow') between each cycle indicates that an *in-situ* EIS measurement has been recorded at each stripping/plating cycle interval of the cell.
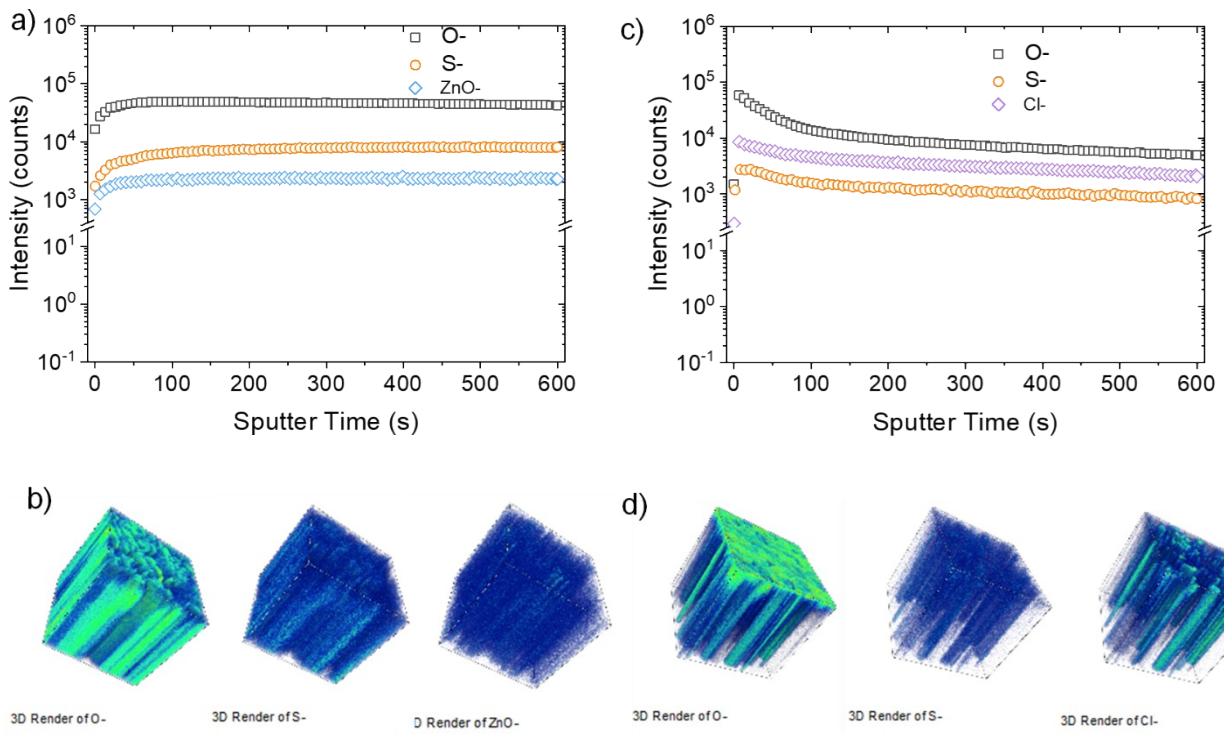
Figure S6. ToF-SIM characterisation of the Zn metal after chronopotentiometry cycling in pristine ZnSO$_4$ (left hand side) and hybrid electrolytes (right hand side). (a) and (b) Depth profiles and 3D rendered mapping images of O-, S- and ZnO- (left to right) anionic specifies on the Zn metal. (c) Depth profiles and (d) 3D mapping images of O-, S- and Cl- anionic species of Zn metal after cycling in hybrid electrolyte.
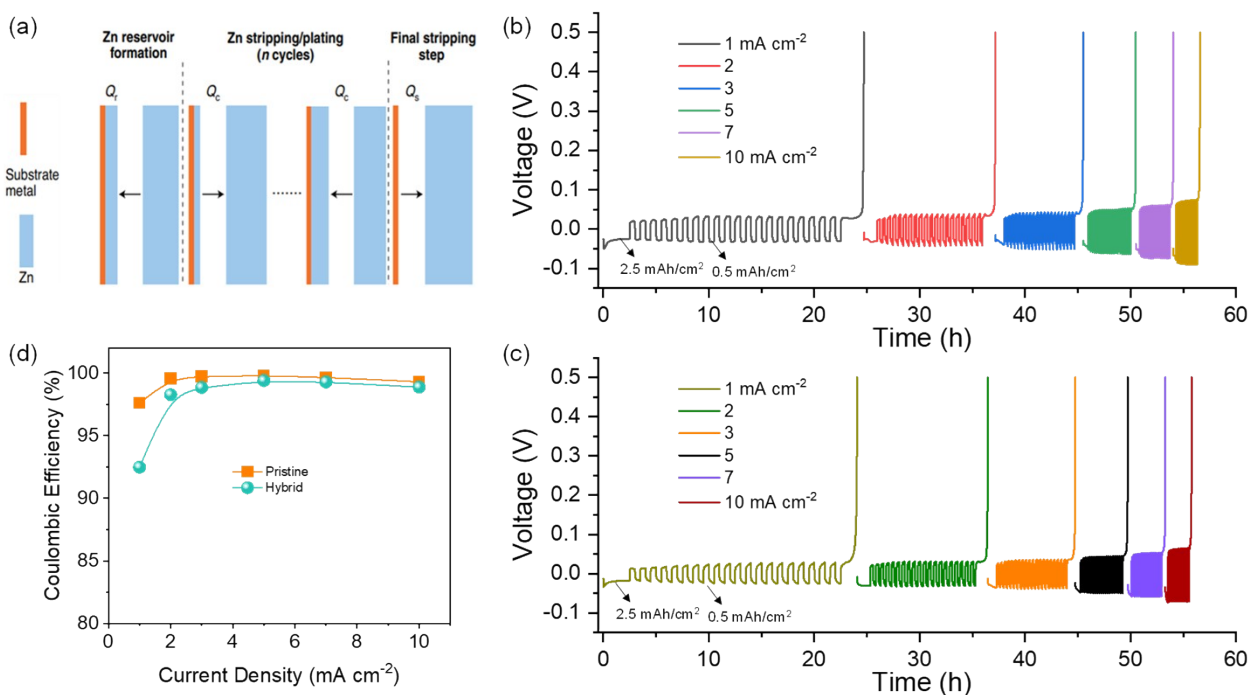
Figure S7. a) Schematic of galvanostatic cycling protocol for evaluating Zn stripping/plating Coulombic efficiency (CE). The plots in b) and c) show the voltage vs. time profile for Cu//Zn cells with pristine and hybrid electrolytes. d) corresponding CE values.

Coulombic efficiency (CE) of Zn//Cu cells using pristine and hybrid electrolytes at different charges ranging from 1-10 mA cm^{-2} was also measured to evaluate the plating/stripping efficiency. For both cells, a given amount of charge (Q_T) is used to deposit Zn onto the Cu substrate first to form a Zn reservoir, then a smaller portion of this charge (Q_c) is used to cycle Zn between working and counter electrodes for 20 cycles. After 20 cycles, a final exhaustive strip of the remaining Zn reservoir is performed to the cut-off voltage of 0.5 V. The final stripping charge (Q_S), corresponding to the quantity of Zn remaining after cycling, is measured. The average CE at different current densities vs. cycles were calculated, as presented in Figure S7. The minimal variation in CE of pristine and hybrid electrolyte illustrate-based Zn//Cu cells illustrate the good Zn plating and stripping efficiency. The average CE is calculated based on the following equation;

$$CE = \frac{20Q_C + Q_S}{20Q_C + Q_t}$$

Pristine Electrolyte		Hybrid Electrolyte	
E_{corr} (mV)	-576.3	E_{corr} (mV)	-567.2
I_{corr} (mA)	6.8	I_{corr} (mA)	5.0
β_a (mV)	223.6	β_a (mV)	231.4
β_c (mV)	250.8	β_c (mV)	230.2

Table S1. Tafel plots fitting values of Zn metal measured in three-electrode system using two different electrolytes, such as pristine ZnSO$_4$ and hybrid electrolyte.
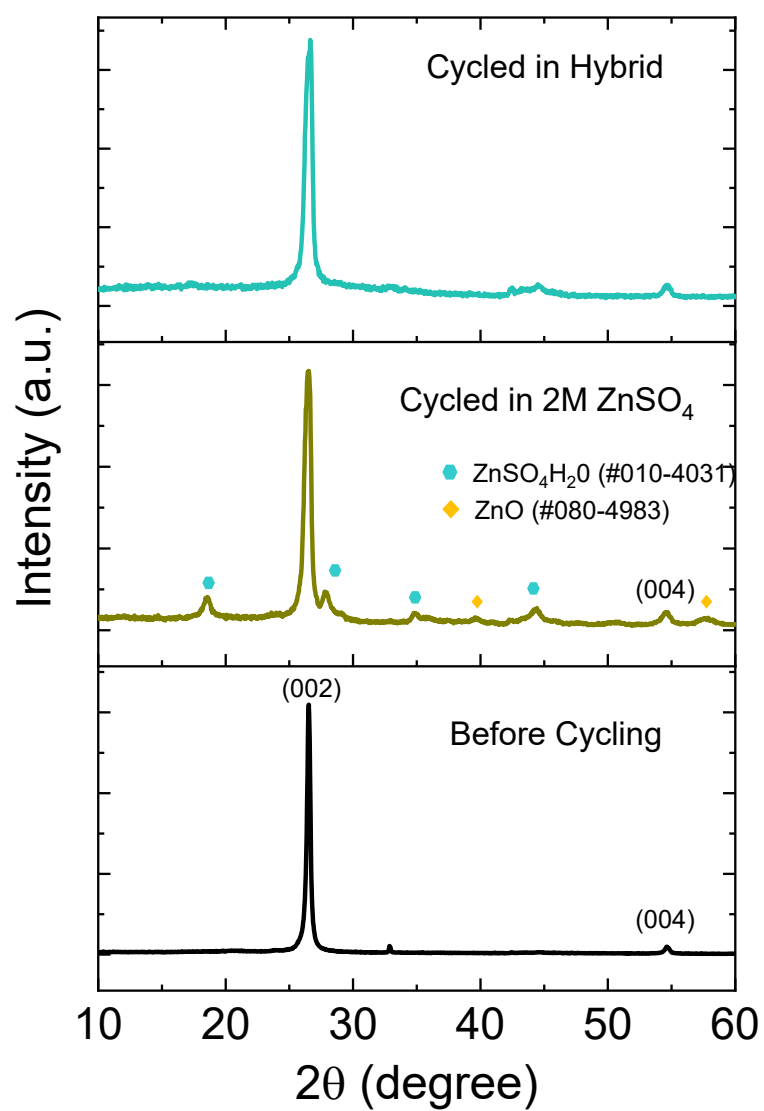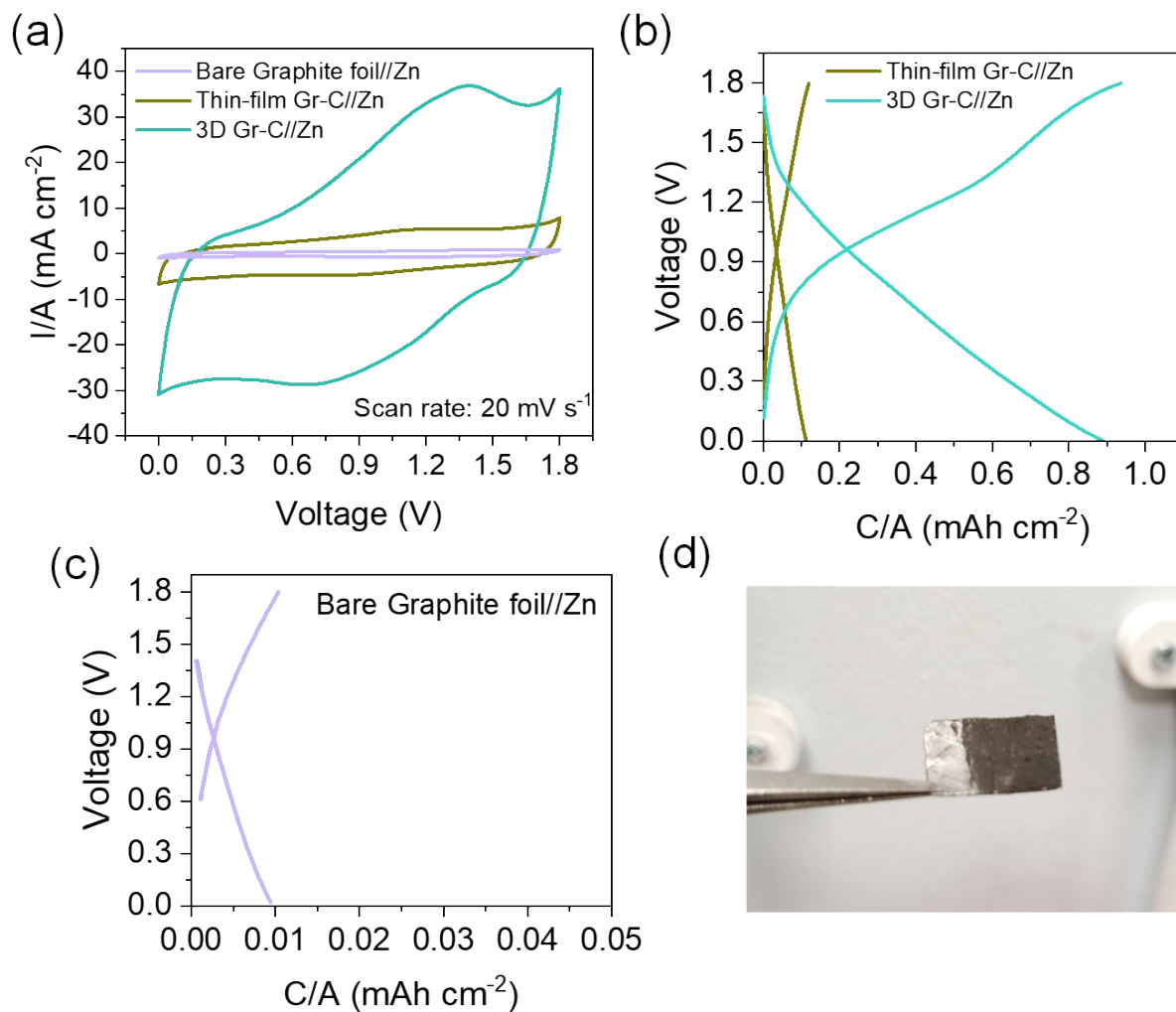
(a)
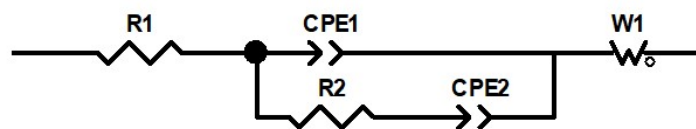
(b)

| Parameters	$R_s/\Omega\ cm^2$	$R_{ct}/\Omega\ cm^2$	$CPE_1/\mu C\ cm^{-2}$	$CPE_2/\mu F\ cm^{-2}$	$W_R/\Omega\ cm^2$
ZnSO$_4$	4.7	0.154	0.254	0.0942	3.5
Hybrid electrolyte	1.9	0.125	0.101	0.0347	3.23

Figure S8. (a) EIS fitting module for ZHCs and (b) EIS parameters obtained from the pristine ZnSO$_4$ and hybrid electrolyte.

Figure S9. *Ex-situ* XRD spectra of 3D Gr-C electrode after cycling in pristine 2M $ZnSO_4$ and hybrid electrolyte.

Figure S10. Comparative (a) CV curves and (b-c) charge-discharge capacities of bare graphite foil//Zn cells with thin-film and 3D printed Gr-C cathode//Zn cells in hybrid electrolyte. d) Photograph of the thin-film Gr-C cathode used in assembling Gr-C//Zn cell. As indicated in the charge-discharge curves of c), the capacity (C/A) contribution from the blank current collector (graphite foil//Zn) is negligible. The high electrochemical active area from the CV curve along with superior charge-discharge capacity (0.88 mAh cm^{-2} vs. 0.11 mAh cm^{-2}) of 3D printed cell demonstrate the feasibility of high energy storage over thin-film based rigid electrodes.
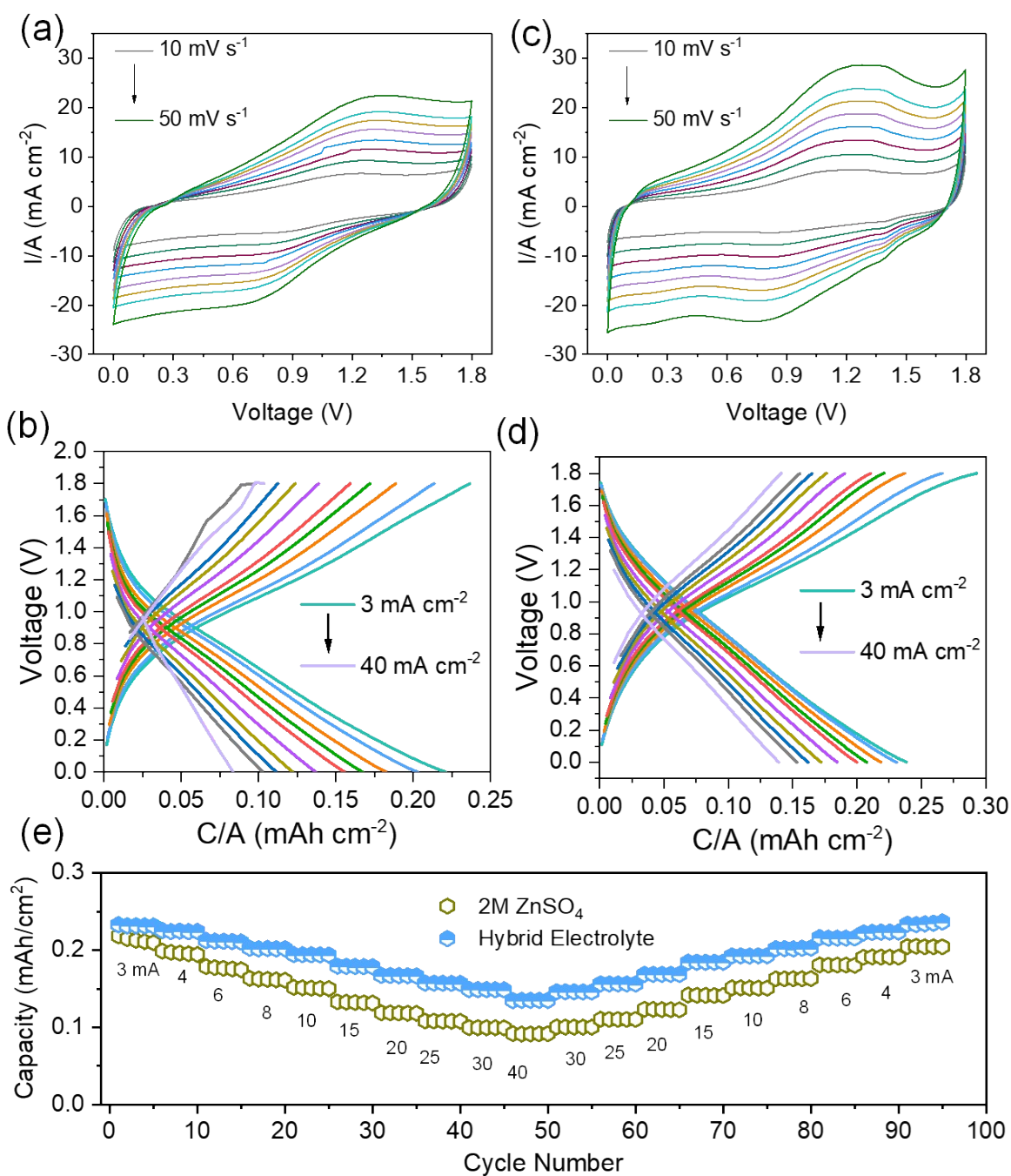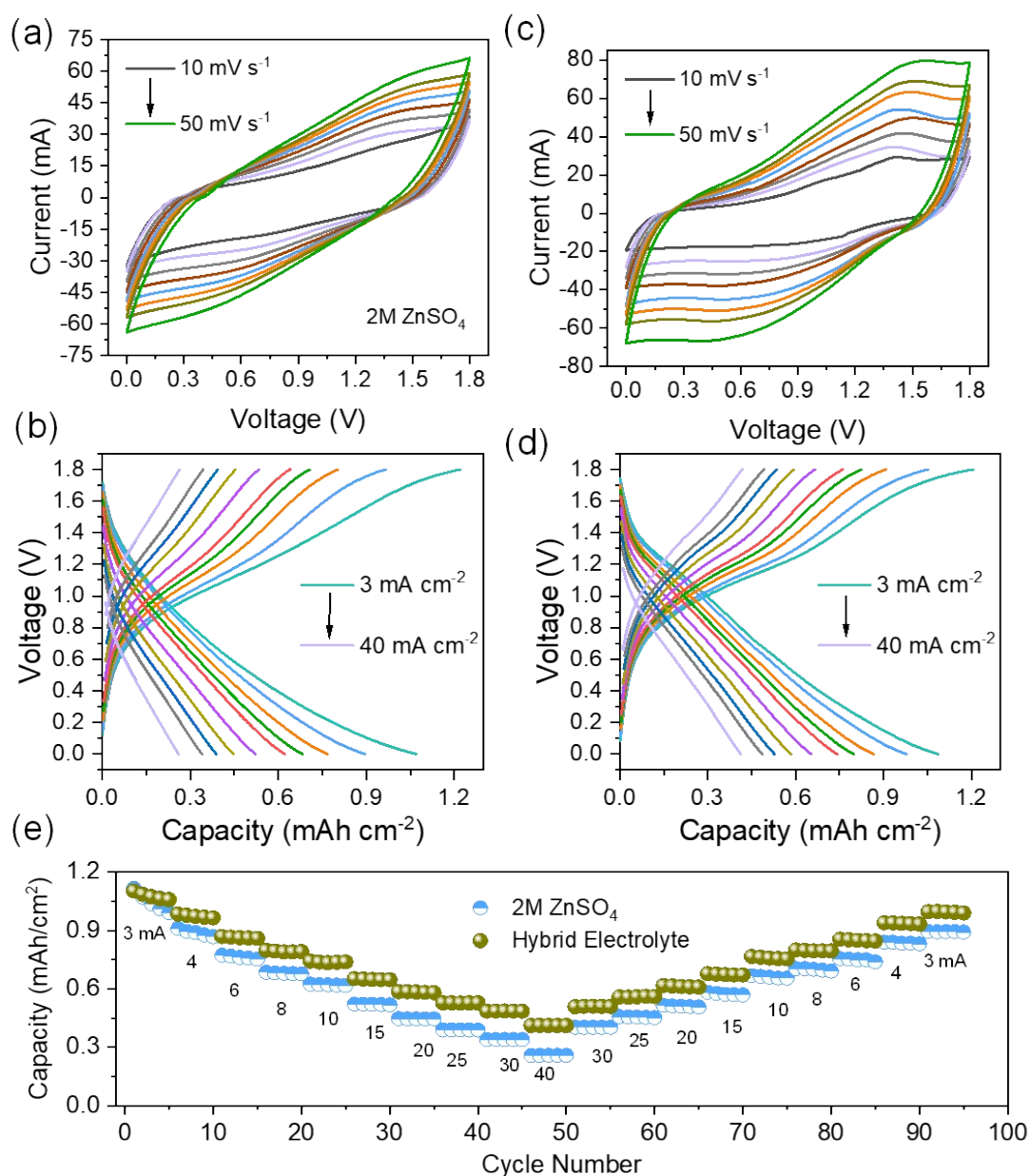
Figure S11. Overall electrochemical properties of 3L Gr-C//Zn cells in pristine and hybrid electrolytes. (a) CV curves and (b) GCD capacity plots of pristine $ZnSO_4$-based ZHCs at various scan rates of 10-50 mV s^{-1} and current densities of 3-40 mA cm^{-2}. (c) CV curves (d) GCD capacities of hybrid electrolyte measured under the different scan rates of 10-50 mV s^{-1} and current densities of 3-40 mA cm^{-2}, respectively. The comparative rate performance of 3L Gr-C//Zn cells analysed using pristine and hybrid electrolyte at different current densities of 3-40 mA cm^{-2}.
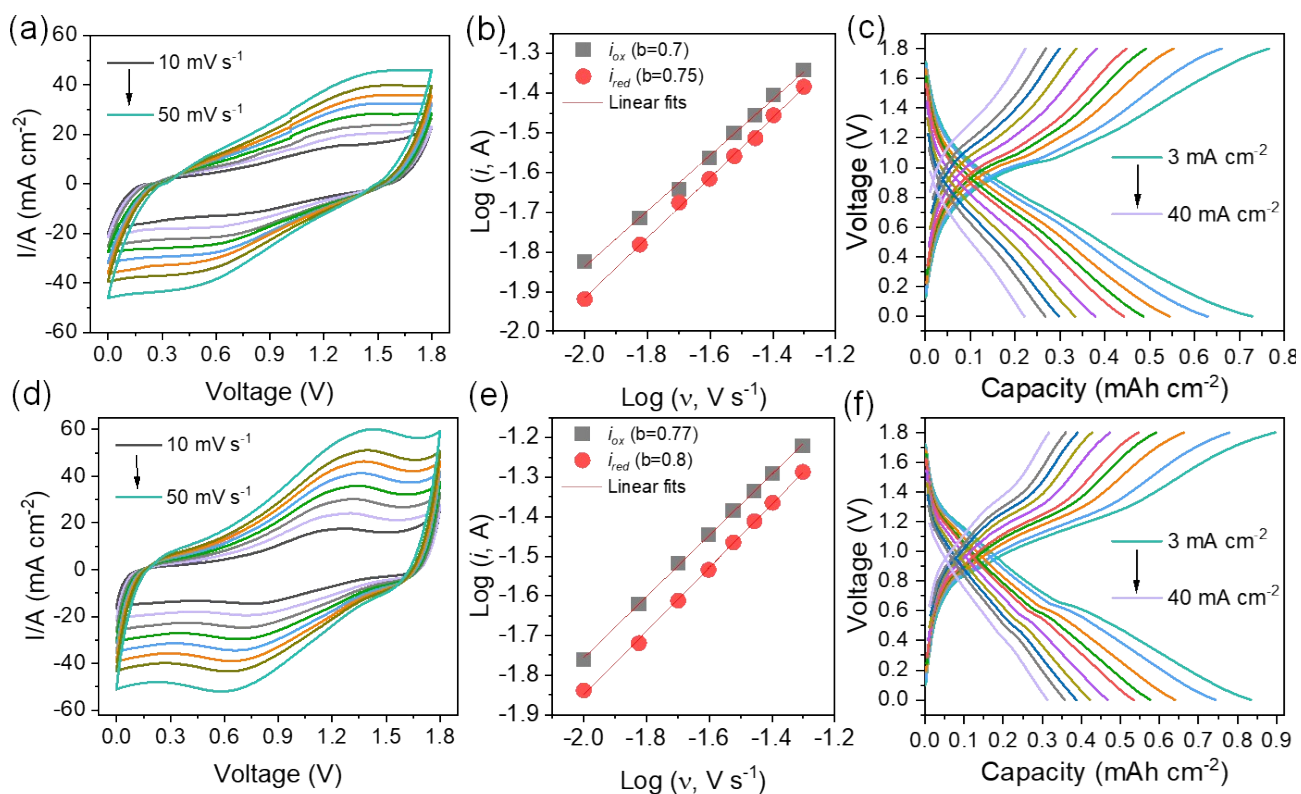
Figure S12. Electrochemical properties of 6L Gr-C//Zn cells measured two-different electrolytes. (a) CV curves and (c) GCD capacity plots of pristine ZnSO$_4$-based ZHCs at various scan rates of 10-50 mV s^{-1} and current densities of 3-40 mA cm^{-2}. (d) CV curves (f) GCD capacities of hybrid electrolyte measured under the different scan rates of 10-50 mV s^{-1} and current densities of 3-40 mA cm^{-2}. b-values obtained *via* the linear fitting of *I/A* transients and scan rates of 6L Gr-C//Zn cell analysed with (b) pristine and (e) hybrid electrolyte, respectively. The b-values obtained from the power law-indicates the possible faradaic and capacitive- process of Gr-C//Zn cell with both anions and cations of ZnSO$_4$ and ZnSO$_4$+NaCl electrolyte.
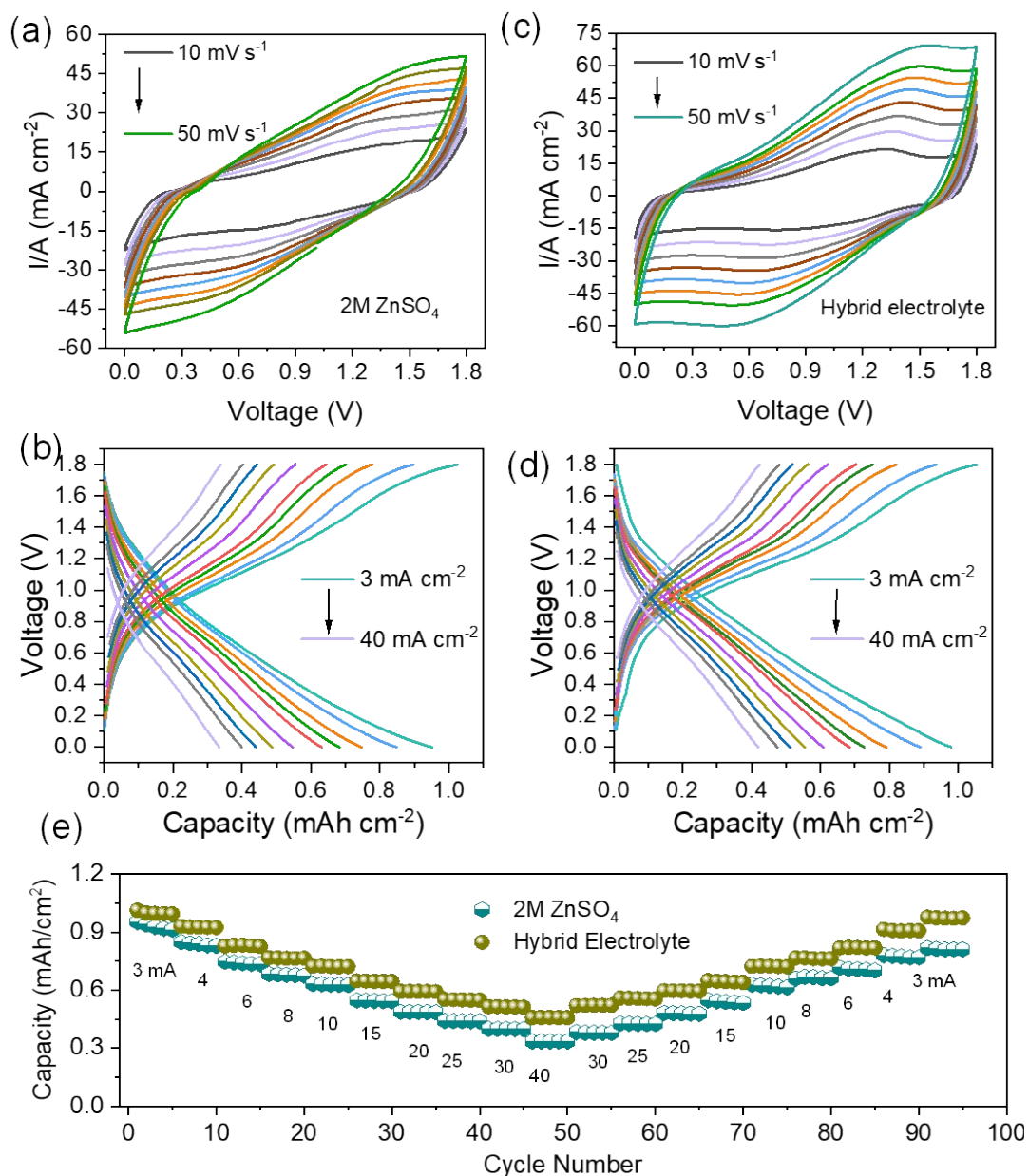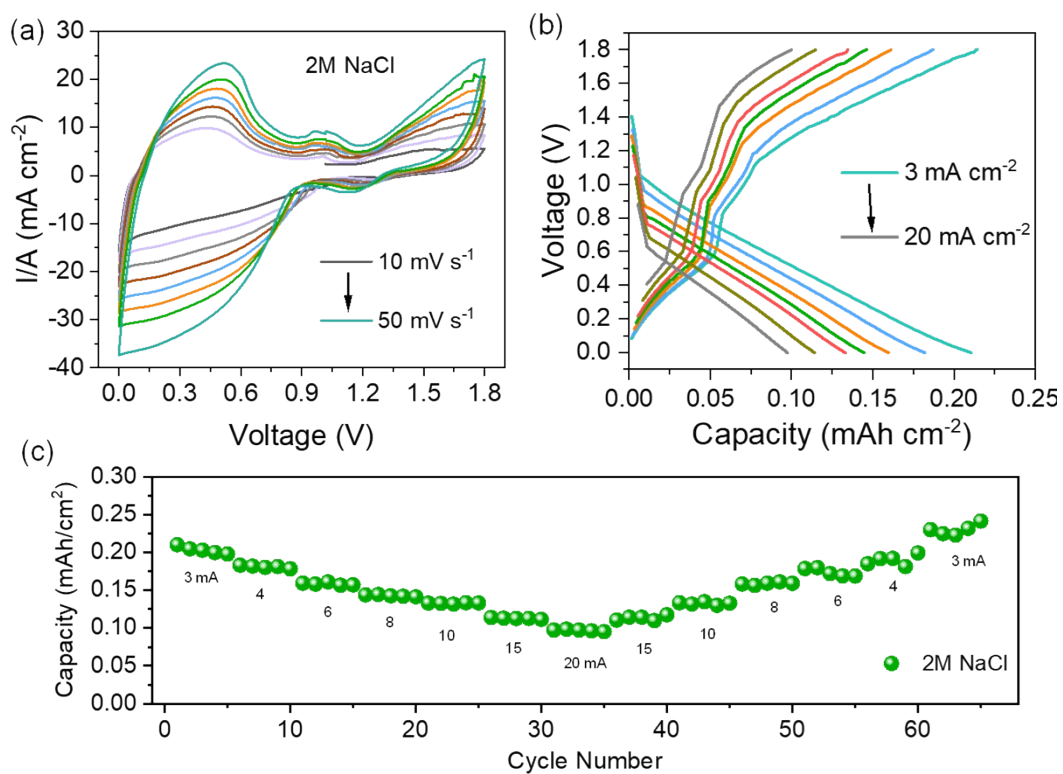
Figure S13. Electrochemical properties of 8L Gr-C//Zn cells analysed in pristine $ZnSO_4$ and hybrid electrolyte. (a) CV curves and (b) GCD capacity plots of pristine $ZnSO_4$-based ZHCs at different scan rates of 10-50 mV s^{-1} and current densities of 3-40 mA cm^{-2}. (c) CV curves (d) GCD capacities of hybrid electrolyte measured under the different scan rates of 10-50 mV s^{-1} and current densities of 3-40 mA cm^{-2}, respectively. The comparative rate performance of 8L Gr-C//Zn cells analysed using pristine and hybrid electrolyte at different current densities of 3-40 mA cm^{-2}.

Figure S14. Detailed electrochemical properties of 12L Gr-C//Zn cells analysed in pristine $ZnSO_4$ and hybrid electrolyte. (a) CV curves and (b) GCD capacity plots of pristine $ZnSO_4$-based ZHCs at different scan rates of 10-50 mV s^{-1} and current densities of 3-40 mA cm^{-2}. (c) CV curves (d) GCD capacities of hybrid electrolyte measured under the different scan rates of 10-50 mV s^{-1} and current densities of 3-40 mA cm^{-2}, respectively. The comparative rate performance of 12L Gr-C//Zn cells analysed using pristine and hybrid electrolyte at different current densities of 3-40 mA cm^{-2}.

Figure S15. Electrochemical properties of 6L Gr-C//Zn cells analysed in 2M NaCl. (a) CV curves and (b) GCD capacity plots measured at different scan rates of 10-50 mV s^{-1} and current densities of 3-20 mA cm^{-2}. (c) Rate performance of corresponding cell at different current densities of 3-20 mA cm^{-2}.
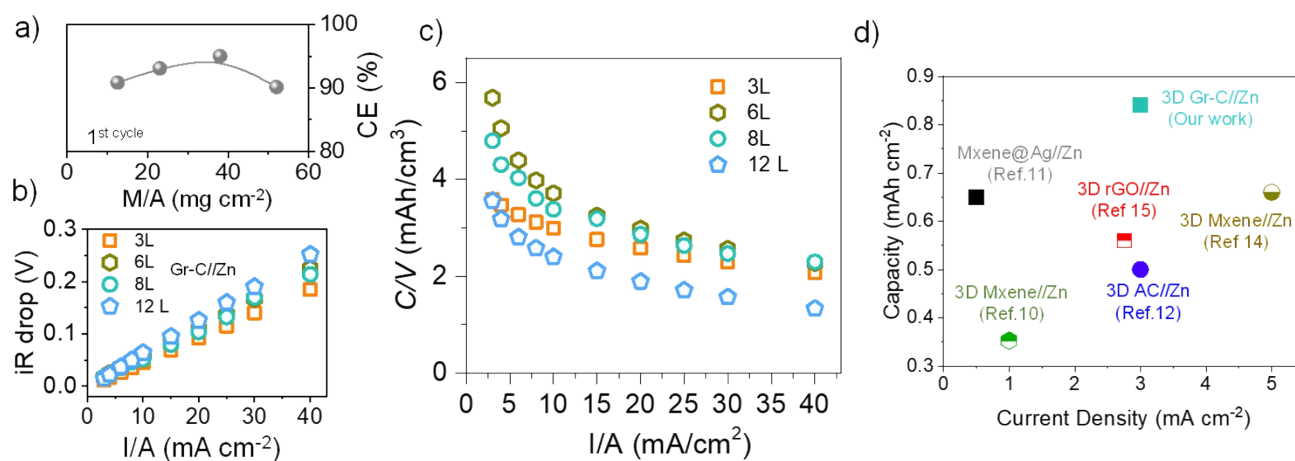
Figure S16. Coulombic efficiencies of 3D Gr-C//Zn cells with varies M/A of cathodes, b) Voltage drop (iR drop) of the corresponding cells up on increasing the charge-discharge I/A's. c) Effect of volumetric capacity on printing layers of hybrid electrolyte-based 3D Gr-C//Zn cells. d) Comparison of areal capacity of our 3D Gr-C//Zn device with previously reported 3D printed Zn-ion capacitors.
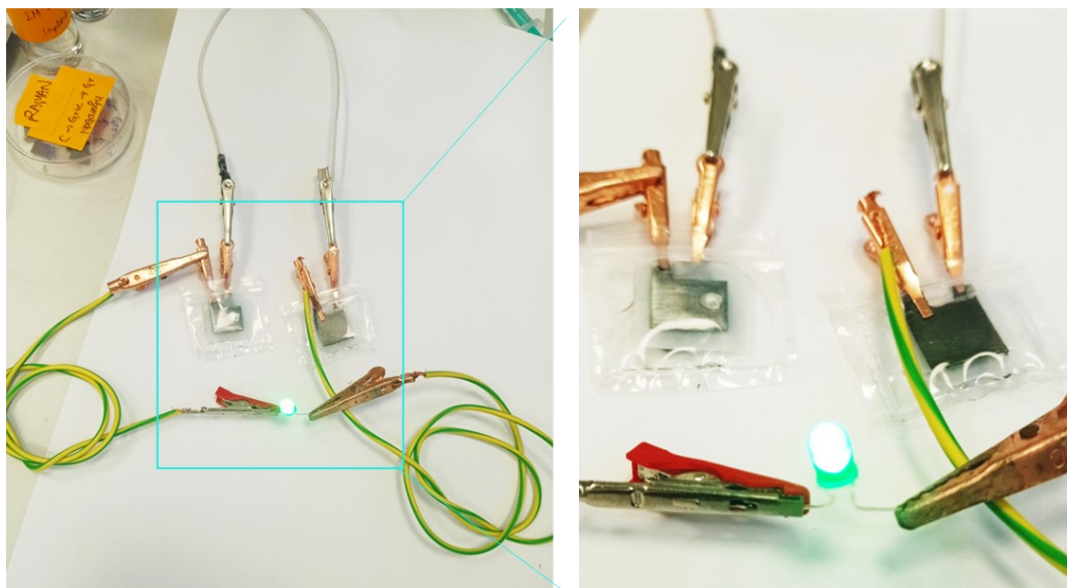
Figure S17. Digital photographs of serially connected 3D 6L Gr-C//Zn cells, successfully illuminating high-voltage (3V) light-emitting diode.

Table S2. Electrochemical performance of previously reported 3D printed microsupercapacitors and metal-ion hybrid capacitors with our 3D Gr-C//Zn hybrid electrolyte based ZHCs.

Energy storage device	Cathode	Anode	Electrolyte	Voltage (V)	E_d (mWh cm^{-2})	P_d (mW cm^{-2})	SI Ref.
Microsupercapacitor	3D CNTs	3D CNTs	PVA-H$_3$PO$_4$	1.0	3.31E-04	10.2672	[3]
Microsupercapaciotr	3D Graphene aerogel	3D Graphene aerogel	6 M KOH	0.8	0.02094	1.54006	[4]
Microsupercapaciotr	3D pristine graphene	3D pristine graphene	1 M LiOH	1.0	0.0512	0.96857	[5]
Microasymmetric supercapacitor	3D V$_2$O$_5$/CNT	3D VN/CNT	PVA-KOH	1.6	0.04162	0.48678	[6]
Microsupercapacitor	3D Ti$_3$C$_2$T$_x$	3D Ti$_3$C$_2$T$_x$	PVA-H$_2$SO$_4$	0.6	0.02583	0.25646	[7]
Microsupercapacitor	3D V$_2$O$_5$/rGO	3D VN/rGO	PVA-LiCl	1.6 V	0.01297	0.32428	[8]
Na-ion microcapacitor	3D N-doped Ti$_3$C$_2$T$_x$	3D activated carbon	1 M NaClO$_4$	4.0 V	1.17118	1.52769	[9]
Zn-ion capacitor	3D MXene	3D CNTs/Zn	2M ZnSO$_4$	1.2 V	0.02995	0.80793	[10]
Zn-ion capacitor	Printed Mxene/Ag	Laser-derived Zn foil	ZnCl$_2$ + NH$_4$Cl	1.4 V	0.227	1.41	[11]
Zn-ion hybrid supercapacitors	3D Activated carbon	ED Zn nanosheets	2 M ZnSO$_4$	1.5 V	0.115	0.16	[12]
Zn-ion hybrid supercapacitors	Printed Calp-carbon	Printed Zn powder	PAM-Zn(CF$_3$SO$_3$)$_2$	1.7 V	0.04	8.2	[13]
Zn-ion hybrid supercapacitors	Patterned Ti$_3$C$_2$T$_x$	ED Zn	6 M ZnCl$_2$	1.4 V	0.5	20	[14]
Zn-ion hybrid capacitors	3D rGO	Zn foil	1M Zn(CF$_3$SO$_3$)$_2$	1.8 V	0.26	0.1	[15]
Zn-ion hybrid capacitor	3D Gr-C composite	Zn foil	2M Zn$_2$SO$_4$+NaCl	1.8 V	0.87	31.72	Our work

Zn: Zinc, ED: Electrodeposition, rGO: reduced graphene oxide, CNT or C: carbon nanotubes, Gr: graphene
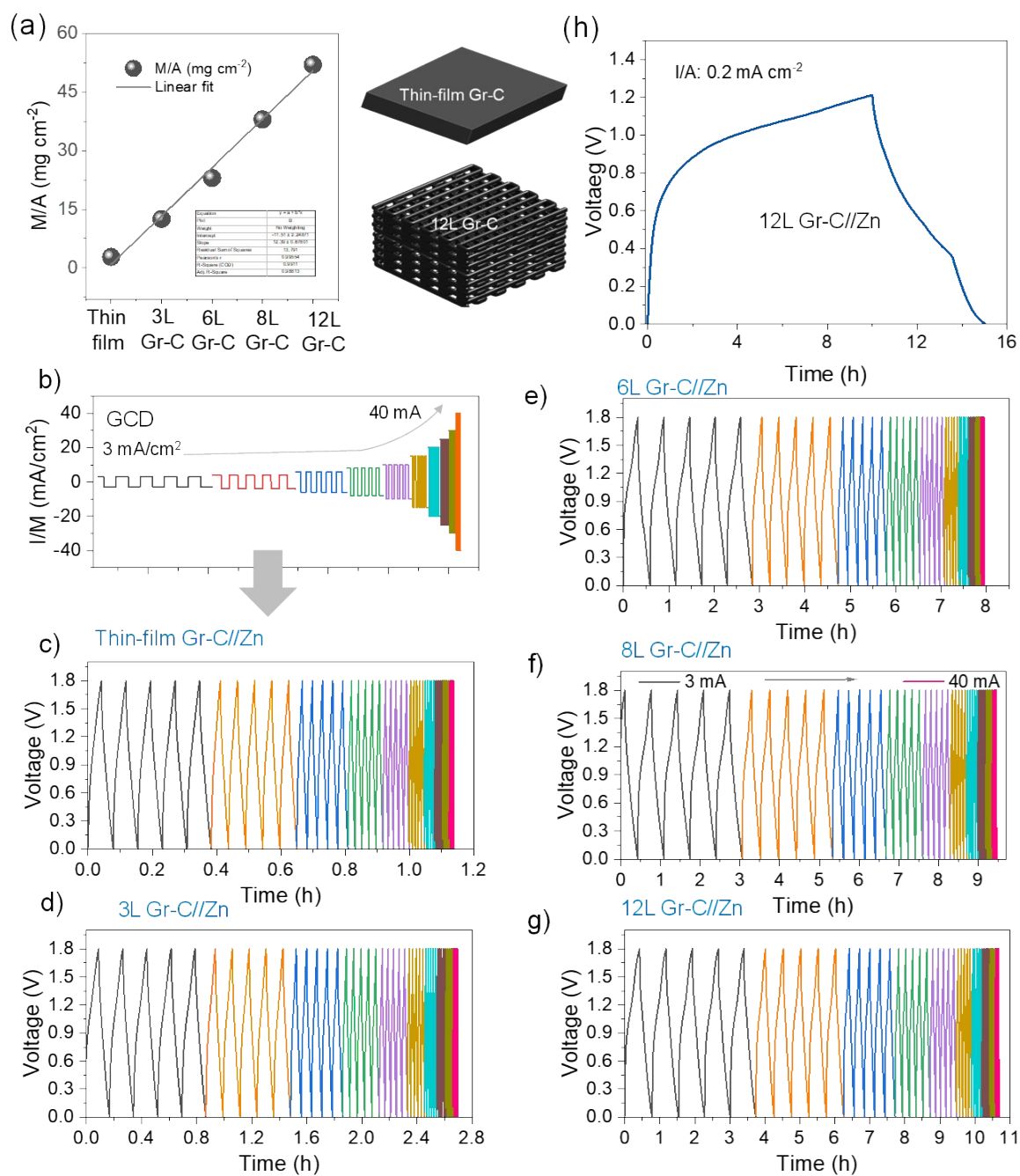
Figure S18. a) Mass loading comparison of thin-film Gr-C and 3D Gr-C cathodes (up to 52 mg cm^{-2}). b) Various charge-discharge current transients (3-40 mA cm^{-2}) used for the GCD process of thin-film-based Gr-C//Zn and 3D Gr-C//Zn cells. Charge-discharge times taken for c) thin-film Gr-C//Zn (□1.2 h), d) 3L Gr-C//Zn (□2.8 h), e) 6L Gr-C//Zn (□ 8 h), f) 8L Gr-C//Zn (□ 9.5 h) and g) 12L Gr-C//Zn (□11 h) cells assembled with hybrid electrolyte, respectively. h) Charge-discharge curve of 12L Gr-C//Zn cell measured at a low-charge discharge I/A of 0.2 mA cm^{-2}. The corresponding plots indicates that the added mass loading of active material on cathode initiate the cell to consume long hours of charge-discharging times. At very low current density of 0.2 mA cm^{-2}, the time taken for the one charge-discharge cycle of 12 L Gr-C//Zn is □15 h (h). These results indicate that the conventional GCD usually take long time to measure the rate performance of high-mass loading ZHCs from low-moderate current densities.

SI References:

1   R. Saito, M. Hofmann, G. Dresselhaus, A. Jorio and M. S. Dresselhaus, *Adv. Phys.*, 2011, **60**, 413–550.

2   M. S. Dresselhaus, G. Dresselhaus, R. Saito and A. Jorio, *Phys. Rep.*, 2005, **409**, 47–99.

3   W. Yu, H. Zhou, B. Q. Li and S. Ding, ACS Appl. Mater. Interfaces, 2017, 9, 4597–4604.

4   X. Tang, H. Zhou, Z. Cai, D. Cheng, P. He, P. Xie, D. Zhang and T. Fan, ACS Nano, 2018, 12, 3502–3511.

5   S. Tagliaferri, G. Nagaraju, A. Panagiotopoulos, M. Och, G. Cheng, F. Iacoviello and C. Mattevi, ACS Nano, 2021, 15, 15342–15353.

6   J. Zhao, Y. Zhang, Y. Huang, J. Xie, X. Zhao, C. Li, J. Qu, Q. Zhang, J. Sun, B. He, Q. Li, C. Lu, X. Xu, W. Lu, L. Li and Y. Yao, Adv. Sci., 2018, 5, 1801114.

7   W. Yang, J. Yang, J. J. Byun, F. P. Moissinac, J. Xu, S. J. Haigh, M. Domingos, M. A. Bissett, R. A. W. Dryfe and S. Barg, Adv. Mater., 2019, 31, 1–8.

8   K. Shen, J. Ding and S. Yang, Adv. Energy Mater., 2018, 8, 1800408.

9   Z. Fan, C. Wei, L. Yu, Z. Xia, J. Cai, Z. Tian, G. Zou, S. X. Dou and J. Sun, ACS Nano, 2020, 14, 867–876.

10   Z. Fan, J. Jin, C. Li, J. Cai, C. Wei, Y. Shao, G. Zou and J. Sun, ACS Nano, 2021, 15, 3098–3107.

11   Z. Cao, H. Hu and D. Ho, Adv. Funct. Mater., 2022, n/a, 2111805.

12   P. Zhang, Y. Li, G. Wang, F. Wang, S. Yang, F. Zhu, X. Zhuang, O. G. Schmidt and X. Feng, Adv. Mater., 2019, 31, 1806005.

13   J. Zeng, L. Dong, L. Sun, W. Wang, Y. Zhou, L. Wei and X. Guo, Nano-Micro Lett., 2020, 13, 19.

14   L. Li, W. Liu, K. Jiang, D. Chen, F. Qu and G. Shen, Nano-Micro Lett., 2021, 13, 100.

15   H. Xu, W. He, Z. Li, J. Chi, J. Jiang, K. Huang, S. Li, G. Sun, H. Dou and X. Zhang, Adv. Funct. Mater., 2022, n/a, 2111131.